Research Article | Vol. 26, No. 24 | 26 Nov 2018 | OPTICS EXPRESS 31983
Optics EXPRESS

Temporally resolved two dimensional temperature field of acoustically excited swirling flames measured by mid-infrared direct absorption spectroscopy

XUNCHEN LIU,[1,*] GUOQING WANG,[1] JIANYI ZHENG,[1] LIANGLIANG XU,[1] SIRUI WANG,[1] LEI LI,[1] AND FEI QI[1]

[1]*Key Laboratory for Power Machinery and Engineering of MOE, School of Mechanical Engineering, Shanghai Jiao Tong University, 800 DongChuan Rd., Shanghai, China*
[*]*liuxunchen@sjtu.edu.cn*

Abstract: The detailed understandings of temperature profiles and flow-flame interaction in unsteady premixed swirling flames are crucial for the development of low emission turbine engines. Here, a phase-locked tomographic reconstruction technique measuring the large absorption cross section of CO_2 at its mid-infrared fundamental band around 4.2 μm is used to acquire the flame temperature and *in situ* CO_2 volume fraction distribution in a turbulent premixed swirling flame under different levels of external acoustic forcing amplitude. The temporally resolved temperature field variation reveals large temperature fluctuation in unsteady premixed swirling flames produced near the nozzle exit due to vortex-driven mixing of surrounding cold gas. The temperature fluctuation quickly dissipates when moving downstream of the flame with the flow velocity of the burnt gas. The accurate high temporal resolution thermodynamic measurements of the phase-locked tomographic thermometry technique reported in this work can be generally applied to periodic reacting flows.

1. Introduction

Swirling flames are important in practical combustors such as gas turbine engines and aeroengine combustors [1, 2]. Confined in a combustion chamber, a swirl-stabilized premixed flame usually consists of a rotating fresh gas cone generated from the swirler, a central recirculation zone generated by the vortex break down that anchors the flame, and an outer recirculation zone, separated by inner and outer shear layers, respectively. Strong velocity gradients are presented at both the outer shear layer and the inner shear layer, where the hot burnt gas and cold unburnt gas meet and form the flame surface. The complex dynamics of swirling flames have been a subject of interest in scientific and engineering research [3]. Flow-flame interaction enables the flame to stabilize under the lean premixed condition, which is important in the development of low emission combustion techniques. Although NOx and soot emission are greatly reduced using premixed lean burn technique, thermoacoustic instability becomes an undesirable problem. Coupling of the flame and acoustic wave leads to unsteady heat release and pressure oscillation which can be destructive to the combustion chamber [4, 5].

In order to understand the unsteady heat release and investigate the inhomogeneous flame temperature distribution, both intrusive and laser based techniques have been used. Most of the micro-thermocouple measurements [6–8] need careful calibration since thermocouple probes generally suffer from radiation heat loss, flow disturbance and insufficient temporal responses particular for unsteady flames. Laser based combustion diagnostics techniques such as laser induced fluorescence [9, 10], coherent anti-Stokes Raman spectroscopy (CARS) [11–13], and absorption spectroscopy [14–19] allow in situ and non-intrusive measurements of temperature in harsh turbulent flames. For the swirling flame study, Halthore et al. [20] and Tangirala et

#344758 https://doi.org/10.1364/OE.26.031983
Journal © 2018 Received 6 Sep 2018; revised 13 Oct 2018; accepted 13 Oct 2018; published 19 Nov 2018

Optics EXPRESS

al. [21] used Rayleigh scattering to measure the temperature distribution in both premixed and non-premixed swirling flames. Single point CARS measurement has been applied to premixed open flame [22], technical swirl combustor [23], swirling sooting flame [24], and swirling spray flame [25]. Keck et al. [26] and Weigand et al. [27] applied Raman scattering in confined gas turbine model combustors. These studies of steady swirling flames show that finite-rate chemistry can lead to a significant deviation from equilibrium temperature and that high temperature area is mainly in the central recirculation zone with large variance around the inner shear layer.

Coupled with acoustic waves, swirling flames oscillate at frequencies from tens to thousands Hz, leading to significant periodic variations of flame structure and temperature profiles that can influence the local heat release and pollutant formation. High fidelity temporally resolved flame temperature measurements are rare for such unsteady flames. A recent study by Arndt et al. [28] showed that a self-excited partially premixed swirling flame has phase-dependent flame temperature variations predominantly close to the nozzle. It was also revealed that a phase-dependent high temperature zone appears in this region because of near-stoichiometric mixture fraction. Besides the self-excited flames, swirling flames perturbed by external acoustic forcing have also been widely used to investigate the relations between heat release and flow oscillation [29–32]. It is necessary to investigate the temperature oscillation in such flames to characterize unstable lean premixed combustion, combustor performance and pollutant emission.

Absorption spectroscopy is an accurate technique that can provide high repetition rate quantitative measurement of gas phase combustion species. Recently, rapid scan direct absorption technique in the mid-infrared range has been reported [33]. The mid-infrared spectral region covers strong fundamental bands of combustion products such as CO_2. Compact room-temperature ICLs and QCLs operating in this region offer unique opportunity for highly accurate and temporally resolved measurement of temperature and CO_2 concentration in a shock tube [34] and in a combustion bomb [35]. Tomographic reconstruction of flame temperature using mid-IR absorption spectroscopy has also been achieved in axisymmetric laminar and turbulent flames [36–40]. The band head at the high frequency end of the of R-branch of CO_2 is particularly interesting because of its immunity to the ambient background absorption, large positive sensitivity to high temperature change, and a number of adjacent transitions that facilitate multi-peak fitting [41, 42].

Although line-of-sight TDLAS measurement has been proved to be capable of monitoring the instability of the swirling flames [43], two dimensional reconstruction of the temperature field that can provide detailed structure and dynamics of the unsteady swirling flames has not been reported. In this paper, we report two-dimensional temperature and CO_2 concentration distribution of an acoustically excited swirling flame obtained by phase-locked tomographic direct absorption spectroscopy at the band head region of CO_2 v_3 fundamental at 2397 cm^{-1}. Turbulent-averaged temperature and CO_2 mole fraction are reported to reveal the onset and propagation of vortex driven temperature fluctuation in the swirling flames under different amplitude of acoustic forcing.

2. Experimental method

Similar to the swirling burner reported by Palies e al. [31], the acoustically forced swirling burner used in this study is schematically shown in Fig. 1(a). It consists of a driver unit, a settling chamber, a contraction ended by a constant diameter duct, a horizontal end piece and a bluff body nozzle. Flow of methane (99.99%, Air Liquid, Shanghai) and air from a compressor is regulated by two thermal mass flow meters (1.0% uncertainty, SevenStar, Beijing) and mixed in the flow pipeline before delivered to the premixing chamber through two opposed stainless steel tube. A porous aluminum plate was used in the premixed chamber to break the large turbulent scales. The premixed gas then crosses a convergent unit to reduce the boundary layer thickness, diminish the level of turbulence and generate a flat velocity profile before flowing through the axial swirler, which consists of eight twisted vanes with NACA 8411 airfoil section that has

Optics EXPRESS

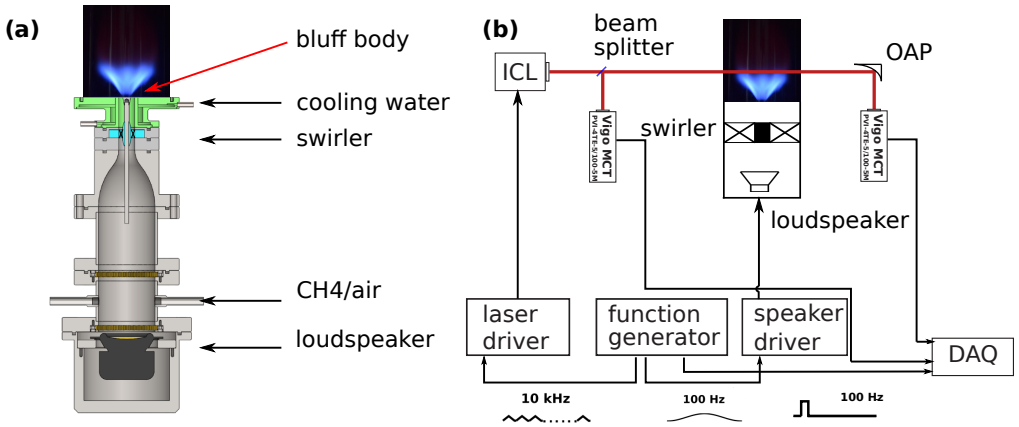

Fig. 1. Schematic drawing of (a) the swirling burner and (b) the experimental setup with the IC laser, MCT detectors, control and data acquisition system and the swirling burner

trailing edge angle varies from 30° at the hub to 60° at the vane tip equispaced on axis core. The swirlers are electrical-discharge machined with 304 stainless steel, which ensures smooth vane surfaces and the minimum thickness at the trailing edge can be as thin as 0.1 mm. The premixed gas then flows through the 20 mm diameter duct with a 10 mm stabilizing bluff body and is burnt once exits the nozzle. A 4 Ohm loudspeaker is mounted at the bottom of the burner to produce the acoustic forcing from upstream. The acoustic forcing was provided by a 200 Hz sinusoidal waveform generated from a 25 MHz two channel function generator (Tektronix AFG3022C) that was amplified by a homemade fix-gain amplifier and sent to the loudspeaker.

In this study, the premixed cold gas flow rate was fixed at 50 SLM while the swirling flame mixture equivalence ratio was fixed at 0.8. The burner was operated under atmospheric condition. The axial component of the cold mixture flow velocity was measured with a one dimensional miniature wire probe Constant Temperature Anemometer (Dantec, MiniCTA) in the constant diameter duct before the flow is rotated by the swirler. The CTA frequency bandwidth is above 10 kHz and the calibration of the CTA was conducted with a stream of dry air in a wind tunnel. Two cases of velocity perturbation $u'/\bar{u} = 0.12$ and $u'/\bar{u} = 0.24$ were studied, where u is the measured flow velocity, $\bar{u}$ is its time average and u' is the perturbation amplitude. The perturbation is in the linear region of the applied sinusoidal waveform amplitude. Figure 2 shows the 100-cycle averaged flow velocity of the $u'/\bar{u} = 0.12$ and $u'/\bar{u} = 0.24$ perturbation.

The mid-IR CO_2 thermometry technique has been recently reported in a study of axisymmetric coflow swirling flames [42]. Briefly, we used a 4.2μm distributed feedback interband cascade laser (Nanoplus, Germany) to probe the bandhead absorption peaks of CO_2 in the swirling flame. The laser injection current and temperature was controlled by a diode laser controller (LDTC0520, Wavelength Electronics, Montana). The laser temperature was tuned to the optimal range to cover the R-branch band head region of the v_3 fundamental at 2397 cm^{-1}. A dual beam absorption scheme was used to account for the laser intensity fluctuation. The probe and reference beams were divided from a calcium fluoride beam splitter and measured by two thermoelectrically cooled mercury cadmium telluride (MCT) photovoltaic detectors (PVI-2TE, Vigo System, Poland). To probe the transmitted signal change is the presence of large thermal radiation from the swirling flames, we restricted the preamplifier bandwidth of the MCT detectors to 100 Hz - 5 MHz, so that the low frequency radiation intensity was filtered out and the linear behavior of the MCT detector was improved. To minimize the thermal gradient effects [44, 45] from the turbulent swirling flame, an 1/2 inch diameter 33 mm focal length off-axis parabolic mirror (MPD01M9-M01, Thorlabs) was closely placed next to the flame to focus the laser beam

Optics EXPRESS

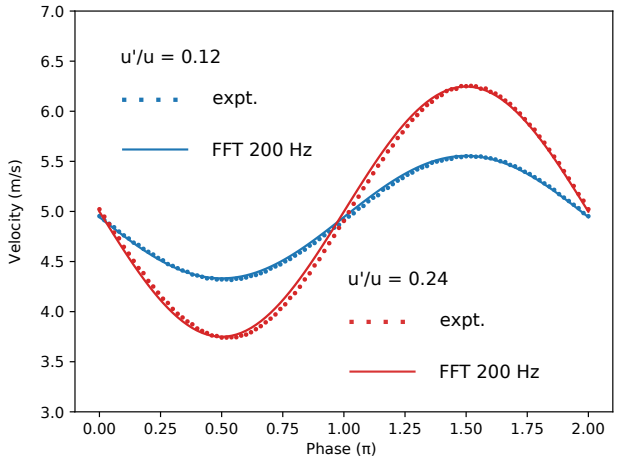

Fig. 2. CTA measured flow velocity with different levels of perturbation amplitude

to the probe beam detector. A 80 mm long solid germanium Fabry-Perot etalon was used for wavelength tuning calibration.

To capture the flame dynamics under acoustic forcing at a few hundred Hz, we used a phase-locked two-dimensional scanning scheme to obtain the temporally resolved tomographic measurement. The schematic experimental setup is depicted in Fig. 1(b). The swirling burner was mounted on vertical and horizontal step motor stages and moved in the 2D plane that is perpendicular to the laser beam so that line-of-sight measurements of the swirling flame can be performed at different heights above the burner (HAB) and radial position. The burner was scanned with 1 mm step in horizontal direction and 2 mm step in vertical direction. At each position during the two-dimensional scan, the two-channel function generator was used to generate synchronized modulation of the acoustic forcing and laser wavelength simultaneously. The injection current was modulated by a 10 kHz triangle waveform from the function generator which was synchronized with the sinusoidal waveform driving the loudspeaker. The amplified voltage signal from the two MCT detectors were then digitized by a 50 MS/s 16 bit digitizer (Gage Applied, USA) which was externally triggered by the sinusoidal waveform driving the loudspeaker and averaged a few hundred cycles over the whole loudspeaker forcing period, which provided phase-averaged measurement of the thermochemical structure of the flames that average out the turbulent fluctuation.

3. Data analysis

The path integrated fractional absorption of the incident laser intensity I_0 is related to temperature, pressure, and number density of the CO_2 molecules in the swirling flames:

$$\frac{I}{I_0} = e^{-\tau} = e^{-\int \mu(r)\,\mathrm{d}l} = e^{-\int k(\nu,T,p)[X]\,\mathrm{d}l} \tag{1}$$

where τ is the dimensionless integrated optical depth; $\mu(r)$ is the attenuation coefficients (per cm) as a function of radius (r) in the axisymmetric swirling flames; $[X]$ is the volume number density of CO_2 (molecule per cm^3); $k(\nu, T, p)$ is the monochromatic absorption coefficient (cm^{-1} per molecule per cm^3) at wavenumber ν, which is the product of the transition line strength $S(\nu, T)$ and the transition lineshape function $f(\Delta\nu, T, p)$.

Assuming a swirling flame with radius R is axisymmetric and steady, Abel inversion was used to obtain the radial distribution of attenuation coefficients $\mu(r)$ at each wavenumber through path

Optics EXPRESS

integrated optical depth τ at lateral positions z:

$$\tau = 2\int_0^{\sqrt{R^2-z^2}} \mu(r)\,dx = 2\int_z^R \mu(r)\,\frac{r}{\sqrt{r^2-z^2}}\,dr \tag{2}$$

In this study, Abel-three-points [46] algorithm with Tikhonov regularization [47] was used to address the inherent ill-conditioned nature of Abel inversion. The local attenuation coefficients array $|\mu\rangle$ can be determined from the path integrated optical depth $|\tau\rangle$ with N number of lateral scanning points.

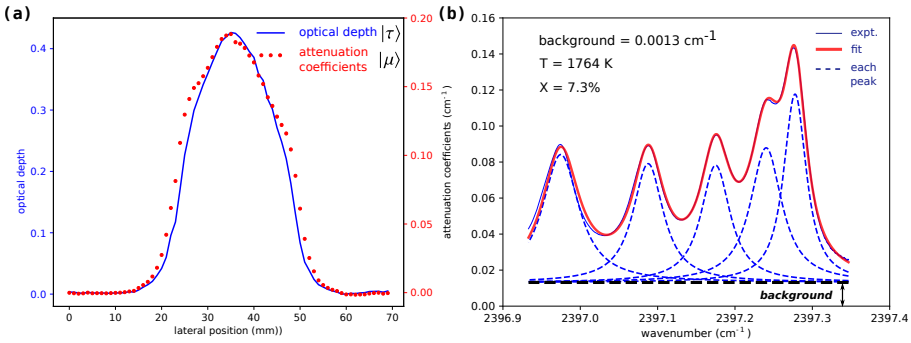

Fig. 3. (a) An example Abel inversion of path integrated optical depth to local attenuation coefficients at HAB = 10 mm and (b) an example attenuation coefficient spectrum at HAB = 10 mm and r = 10 mm of the swirling flame.

$$\mathbf{A_{ATP}}\,|\mu\rangle = |\tau\rangle; \qquad \lambda\,\mathbf{L}\,|\mu\rangle = 0 \tag{3}$$

in which $\mathbf{A_{ATP}}$ is the Abel-three-points projection matrix of dimension N; λ is regularization parameter; $\mathbf{L}$ is the gradient operator of dimension $(N-1)\times N$ to decrease the amplified noise produced from the inversion process. A typical Tikhonov regularization Abel inversion at the absorption peak wavenumber is shown in Fig. 3(a).

Once the local attenuation coefficients spectra of each lateral position and HAB at *each wavenumber* is determined from the Abel inversion, the local temperature and CO_2 mole fraction can be obtained. A typical local attenuation coefficient spectrum is shown in Fig. 3(b). The experimental spectra generally have good signal to noise ratio, showing that the Tikhonov regulated Abel inversion scheme can control the noise amplification in the inversion process. One should note that the experimental data in this study is taken from phase averaging of the turbulent flow in open air. The turbulent averaged absorption peaks are fitted using Voigt lineshape function $f_{\text{Voigt}}(\nu;\nu_0,T,p)$ which is evaluated as the real part of the Faddeeva function $w(z)$ [48]. The turbulent averaged spectra can be fitted with an uniform background and five major peaks, taking into account that the other high J transitions mainly overlap with the five major peaks. We used a high temperature static cell to calibrate the carbon dioxide absorption cross-section up to 1600 K and compared with the simulated spectra using HITRAN 2016 database to correct for the underestimation of the line strength by the database [42]. The corrected major peak area was then used to derive the turbulent averaged temperature and carbon dioxide mole fraction by Levenberg-Marquardt multi-spectra least-square fit using the same strategy as Villarreal *et al.* [41,42]. We estimated the uncertainties of the calibration corrected thermometry technique based on the uncertainty of the measured absorbance values and the calibration tube accuracy. The fitted temperatures have uncertainties mostly below 5% and the concentration uncertainties are around 10%.

Optics EXPRESS

4. Results and discussion

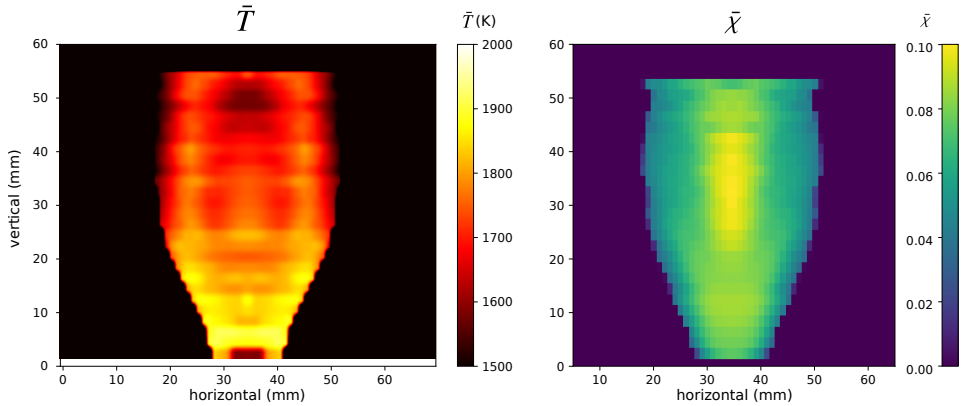

Fig. 4. Mean and standard deviation of temperature and CO_2 mole fraction field measurement

First, the temperature field and CO_2 mole fraction distribution of unperturbed swirling flame was studied. A photograph of the unmodulated lean premixed swirling flame with flow rate 50 SLM and equivalence ratio at $\phi = 0.8$ is shown in Fig. 1. Figure 4 shows the mean and standard deviation of temperature field and CO_2 mole fraction distribution of the flame from 100 continuous measurements. It can be seen that the swirling flame has a V-shape high temperature region at the flame root near the nozzle exit and along the inner shear layer region where flame surfaces exist. The burnt gas temperature gradually decreases as the high temperature region extends to the downstream of the flame. A high temperature central recirculation zone is also clearly visible, but the recirculated burnt gas temperature is lower than the flame surface temperature. On the other hand, the CO_2 mole fraction measurement in Fig. 4 shows that the central recirculation zone has a higher concentration of the combustion product CO_2 than the V-shaped flames surface area. Since the phase-locked measurement was averaged a few hundred cycles at each point, most of the turbulent fluctuation was averaged out and the precision of the continuous measurement of the temperature and CO_2 concentration field is typically around 1%. The temperature field measurement has larger variance at the inner shear layer region with large velocity gradient and the corresponding center line due to the ill-conditioned Abel inversion.

Next, the temperature and CO_2 mole fraction field of acoustically excited swirling flames are studied. The lean premixed flame was applied with a 200 Hz acoustic perturbation with perturbation amplitude u'/u at 12% and 24%. With the 0.1 ms temporal resolution measurement, Fig. 5 presents the phase resolved two-dimensional temperature field for both cases. The temporally resolved two-dimensional temperature field reveals that the flow-flame interactions are mainly driven by large vortex generated by the acoustic forcing. Periodic flame dynamics in a complete 5 ms cycle can be roughly divided into inception stage and mixing stage. During the *inception stage*, a high-temperature zone appears close to nozzle. At the same time, the vortex roll-up exits the bluff body and carries cold gas near the nozzle exit. It can be clearly seen that a vortex is formed due to cold air entrainment. During the following *mixing stage*, the cold gas is mixed into the flame by vortex breaks-down, forming a low temperature gap that propagates downstream of the flame. At the same time, a new vortex has exited the nozzle which will push the low temperature gap downstream during the next inception stage. The large phase-dependent temperature variations we observed agree well with the recent Raman measurement of partially premixed swirling flames [28], in which the high temperature zone near the nozzle exit is above 1900 K and appears during the inception state of the cycle. Comparing the two perturbation amplitudes, we can see that 24% perturbation amplitude produces larger vortex and greater level

Optics EXPRESS

of cold gas mixing. The two dimensional concentration field show similar flow structure. CO_2 is mainly generated by the high temperature zone during the vortex roll-up. The complete 10 ms time sequence of the temperature and CO_2 mole fraction measurements with 0.1 ms resolution for both 12% and 24% perturbation amplitude can be found in Visualization 1, Visualization 2, Visualization 3, and Visualization 4.

Another feature we observed is that overall the average temperature of the perturbed flame is lower than the unmodulated state case in Fig. 4. This is because of the mixing of the high temperature burnt gas with surrounding cold air during the mixing stage. To further study the unsteady heat release and inhomogeneous temperature dynamics, we examine the detailed temperature variation at different radial position and HAB of the flame in Fig. 6. Extensive information can be drawn comparing the temporally resolved temperature measurement. Phase dependent sharp temperature variations are produced close to the nozzle exit around HAB=10 to HAB = 20 mm. Vary sharp drop and increase of flame temperature indicates the passing of a forced flame surface in this area. It should be noted that calibration of the thermometry technique using high temperature tube was up to 1600 K and the fit-obtained temperature values above 2000 K are not reliable. However, valuable conclusions can be qualitatively drawn from the flame temperature variations. In the temporal variation plots shown in Fig. 6, it can be seen that the vortex driven mixing of cold gas brings down the flame temperature and is followed by an increase of flame temperature when the cold gas gap moves up. There is usually a top hat stage when the flame temperature maintains close to the unmodulated state temperature. We can see that the temporal variation profiles of both the 12% perturbation and 24% perturbation amplitude are quite similar, showing the inherent similarities of their acoustically perturbed flow structure.

The temperature fluctuation quickly decreases downstream and to the larger radius of the flame as the acoustical perturbation dissipates. During the propagation of the flame perturbation, the average temperature at most heights, especially at the downstream of the acoustically excited flames is lower than the unperturbed flame due to mixing of surrounding cold air. However, the acoustically excited flames extend to positions outside the unmodulated flame, for example at 20 mm from the flame center shown in Fig. 6, which further demonstrates the effect of the acoustic induced mixing. Here, we can estimate that the wavelength of the temperature fluctuation is around 30 mm and the propagation velocity of the thermodynamic structure downstream is around 6 m/s, which is close to the flow velocity of the burnt gas. We note that the forced propagation speed is faster during the inception stage and is slower during the mixing stage. It is clearly shown that unstable combustion produces local inhomogeneity and fluctuation of gas temperature both at the flame front and downstream of the flame. It should also be noted that the sharp increase of flame temperature is associated with accelerated propagation velocity downstream of the flame, indicating that the vortex driven flame surface stretch and squeeze may lead to both increase and decrease of flame temperature.

Optics EXPRESS

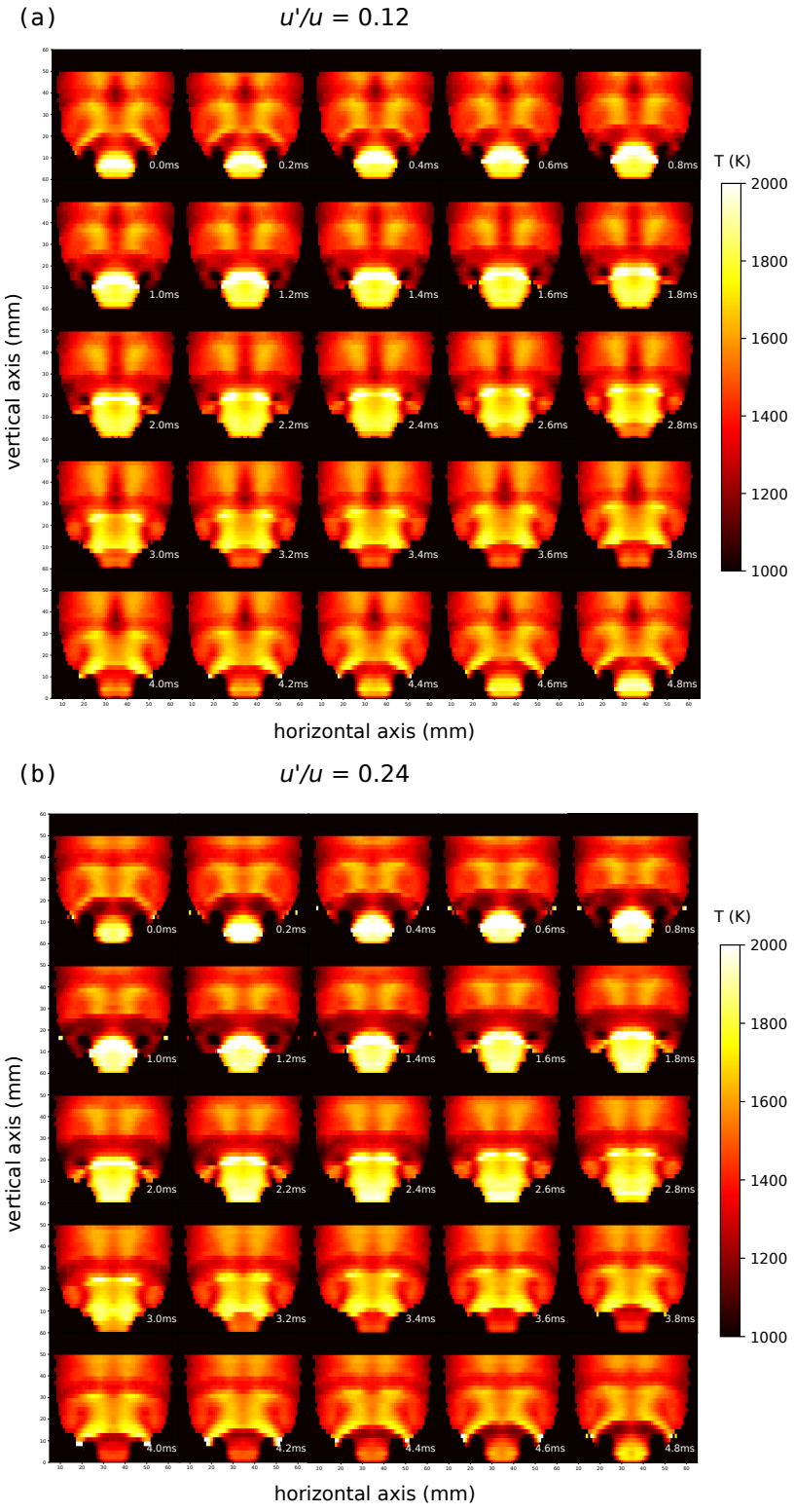

Fig. 5. Temporally resolved flame temperature field with acoustic perturbation amplitude $u'/u = 12\%$ and $u'/u = 24\%$ at different phases

Optics EXPRESS

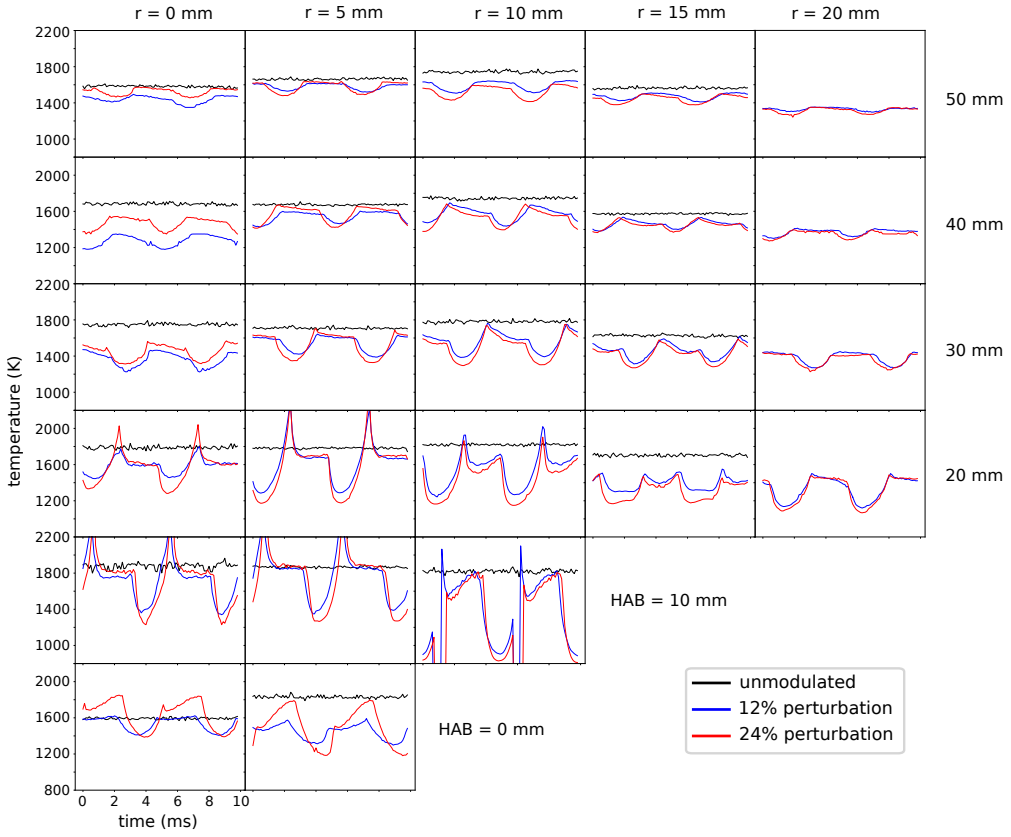

Fig. 6. Temporally resolved flame temperature variations at different heights above the burner and radial positions.

Optics EXPRESS

5. Summary and outlook

A phase-locked tomographic thermometry technique based on mid-infrared direct absorption spectroscopy of CO_2 in the v_3 fundamental band was used to obtained the two dimensional temperature and CO_2 mole fraction field in both unmodulated state and acoustically excited swirling flames. The temporally resolved temperature field measurement agrees well with Raman scattering measurement with detailed dynamics, showing that the perturbation cycle consists of an inception stage and a mixing stage which produce the vortex-driven mixing of hot burnt gas with surrounding cold air. Temperature fluctuations is mainly produced near the nozzle exit and dissipates downstream of the flame at the flow speed of the burnt gas.

The temporal profiles of flame temperature indicate a high temperature accelerated flame surface moving out of nozzle. Further studies of the flow field and flame surface variation are required to elucidate the detailed mechanism of stretch effect to the premixed flame temperature [49, 50]. Temperature and concentration profiles are important characteristics to understand the flame structure and dynamics. The phase-locked thermometry technique reported in this work demonstrates the capability of mid-IR direct absorption spectroscopy to provide accurate measurement of thermodynamic structures that facilitate the study of unsteady reacting flows such as combustion instability.

Funding

National Natural Science Foundation of China (NSFC) (51606123, 91541201, 51676126); Open Research Fund of the State Key Laboratory of Precision Spectroscopy, East China Normal University (sklps2017-7).

References

1. T. C. Lieuwen and V. Yang, *Combustion Instabilities In Gas Turbine Engines: Operational Experience, Fundamental Mechanisms, and Modeling*, Progress in Astronautics and Aeronautics (American Institute of Aeronautics and Astronautics, 2006).
2. I. Chterev, C. W. Foley, D. Foti, S. Kostka, A. W. Caswell, N. Jiang, A. Lynch, D. R. Noble, S. Menon, J. M. Seitzman, and T. C. Lieuwen, "Flame and Flow Topologies in an Annular Swirling Flow," Combust. Sci. Technol. **186**, 1041–1074 (2014).
3. S. Candel, D. Durox, T. Schuller, J.-F. Bourgouin, and J. P. Moeck, "Dynamics of Swirling Flames," Annu. Rev. Fluid Mech. **46**, 147–173 (2014).
4. Y. Huang and V. Yang, "Dynamics and stability of lean-premixed swirl-stabilized combustion," Prog. Energy Combust. Sci. **35**, 293–364 (2009).
5. T. Poinsot, "Prediction and control of combustion instabilities in real engines," Proc. Combust. Inst. **36**, 1–28 (2017).
6. A. V. Singh, A. Eshaghi, M. Yu, A. K. Gupta, and K. M. Bryden, "Simultaneous time-resolved fluctuating temperature and acoustic pressure field measurements in a premixed swirl flame," Appl. Energy **115**, 116–127 (2014).
7. X. Zhu, R. Li, D. Li, P. Zhang, and R. Qian, "Experimental study and RANS calculation on velocity and temperature of a kerosene-fueled swirl laboratory combustor with and without centerbody air injection," Int. J. Heat Mass Transf. **89**, 964–976 (2015).
8. A. M. Elbaz and W. L. Roberts, "Investigation of the effects of quarl and initial conditions on swirling non-premixed methane flames: Flow field, temperature, and species distributions," Fuel **169**, 120–134 (2016).
9. C. Schulz and V. Sick, "Tracer-LIF diagnostics: quantitative measurement of fuel concentration, temperature and fuel/air ratio in practical combustion systems," Prog. Energy Combust. Sci. **31**, 75–121 (2005).
10. B. R. Halls, P. S. Hsu, S. Roy, T. R. Meyer, and J. R. Gord, "Two-color volumetric laser-induced fluorescence for 3d OH and temperature fields in turbulent reacting flows," Opt. Lett. **43**, 2961–2964 (2018).
11. A. Bohlin and C. J. Kliewer, "Communication: Two-dimensional gas-phase coherent anti-Stokes Raman spectroscopy (2d-CARS): Simultaneous planar imaging and multiplex spectroscopy in a single laser shot," The J. Chem. Phys. **138**, 221101 (2013).
12. J. D. Miller, M. N. Slipchenko, J. G. Mance, S. Roy, and J. R. Gord, "1-kHz two-dimensional coherent anti-Stokes Raman scattering (2d-CARS) for gas-phase thermometry," Opt. Express **24**, 24971–24979 (2016).
13. W. D. Kulatilaka, H. U. Stauffer, J. R. Gord, and S. Roy, "One-dimensional single-shot thermometry in flames using femtosecond-CARS line imaging," Opt. Lett. **36**, 4182–4184 (2011).
14. L. Ma, X. Li, S. T. Sanders, A. W. Caswell, S. Roy, D. H. Plemmons, and J. R. Gord, "50-kHz-rate 2d imaging of temperature and H2o concentration at the exhaust plane of a J85 engine using hyperspectral tomography," Opt. Express **21**, 1152–1162 (2013).

Optics EXPRESS

15. X. An, T. Kraetschmer, K. Takami, S. T. Sanders, L. Ma, W. Cai, X. Li, S. Roy, and J. R. Gord, "Validation of temperature imaging by H_2o absorption spectroscopy using hyperspectral tomography in controlled experiments," Appl. Opt. **50**, A29 (2011).
16. X. An, M. S. Brittelle, P. T. Lauzier, J. R. Gord, S. Roy, G.-H. Chen, and S. T. Sanders, "Demonstration of temperature imaging by H_2O absorption spectroscopy using compressed sensing tomography," Appl. Opt. **54**, 9190–9199 (2015).
17. C. Liu, L. Xu, F. Li, Z. Cao, S. A. Tsekenis, and H. McCann, "Resolution-doubled one-dimensional wavelength modulation spectroscopy tomography for flame flatness validation of a flat-flame burner," Appl. Phys. B **120**, 407–416 (2015).
18. C. S. Goldenstein, R. M. Spearrin, J. B. Jeffries, and R. K. Hanson, "Infrared laser-absorption sensing for combustion gases," Prog. Energy Combust. Sci. **60**, 132–176 (2017).
19. C. Liu and L. Xu, "Laser absorption spectroscopy for combustion diagnosis in reactive flows: A review," Appl. Spectrosc. Rev. pp. 1–44 (2018).
20. R. N. Halthore and F. C. Gouldin, "Laser scattering measurements for gas densities in a swirling flow combustor," AIAA J. **24**, 1129–1136 (1986).
21. V. Tangirala and J. F. Driscoll, "Temperatures within Non-premixed Flames: Effects of Rapid Mixing Due to Swirl," Combust. Sci. Technol. **60**, 143–162 (1988).
22. A. Bohlin, E. Nordström, H. Carlsson, X.-S. Bai, and P.-E. Bengtsson, "Pure rotational CARS measurements of temperature and relative O2-concentration in a low swirl turbulent premixed flame," Proc. Combust. Inst. **34**, 3629–3636 (2013).
23. S. Kampmann, T. Seeger, and A. Leipertz, "Simultaneous coherent anti-Stokes Raman scattering and two-dimensional laser Rayleigh thermometry in a contained technical swirl combustor," Appl. Opt. **34**, 2780–2786 (1995).
24. K. P. Geigle, M. Köhler, W. O'Loughlin, and W. Meier, "Investigation of soot formation in pressurized swirl flames by laser measurements of temperature, flame structures and soot concentrations," Proc. Combust. Inst. **35**, 3373–3380 (2015).
25. L. M. L. Cantu, J. Grohmann, W. Meier, and M. Aigner, "Temperature measurements in confined swirling spray flames by vibrational coherent anti-stokes Raman spectroscopy," Exp. Therm. Fluid Sci. **95**, 52–59 (2018).
26. O. Keck, W. Meier, W. Stricker, and M. Aigner, "Establishment of a Confined Swirling Natural Gas/Air Flame as a Standard Flame: Temperature and Species Distributions from Laser Raman Measurements," Combust. Sci. Technol. **174**, 117–151 (2002).
27. P. Weigand, W. Meier, X. R. Duan, W. Stricker, and M. Aigner, "Investigations of swirl flames in a gas turbine model combustor: I. Flow field, structures, temperature, and species distributions," Combust. Flame **144**, 205–224 (2006).
28. C. M. Arndt, M. Severin, C. Dem, M. Stöhr, A. M. Steinberg, and W. Meier, "Experimental analysis of thermo-acoustic instabilities in a generic gas turbine combustor by phase-correlated PIV, chemiluminescence, and laser Raman scattering measurements," Exp. Fluids **56**, 1–23 (2015).
29. B. D. Bellows, M. K. Bobba, J. M. Seitzman, and T. Lieuwen, "Nonlinear Flame Transfer Function Characteristics in a Swirl-Stabilized Combustor," J. Eng. for Gas Turbines Power **129**, 954 (2007).
30. B. D. Bellows, M. K. Bobba, A. Forte, J. M. Seitzman, and T. Lieuwen, "Flame transfer function saturation mechanisms in a swirl-stabilized combustor," Proc. Combust. Inst. **31**, 3181–3188 (2007).
31. P. Palies, D. Durox, T. Schuller, and S. Candel, "The combined dynamics of swirler and turbulent premixed swirling flames," Combust. Flame **157**, 1698–1717 (2010).
32. D. Durox, J. P. Moeck, J.-F. Bourgouin, P. Morenton, M. Viallon, T. Schuller, and S. Candel, "Flame dynamics of a variable swirl number system and instability control," Combust. Flame **160**, 1729–1742 (2013).
33. X. Liu, Y. Xu, Z. Su, W. S. Tam, and I. Leonov, "Jet-cooled infrared spectra of molecules and complexes with a cw mode-hop-free external-cavity QCL and a distributed-feedback QCL," Appl. Phys. B **102**, 629–639 (2010).
34. R. M. Spearrin, W. Ren, J. B. Jeffries, and R. K. Hanson, "Multi-band infrared CO2 absorption sensor for sensitive temperature and species measurements in high-temperature gases," Appl. Phys. B **116**, 855–865 (2014).
35. G. Wang, B. Mei, X. Liu, G. Zhang, Y. Li, and F. Qi, "Investigation on spherically expanding flame temperature of n-butane/air mixtures with tunable diode laser absorption spectroscopy," Proc. Combust. Inst. (2018).
36. J. J. Girard, R. M. Spearrin, C. S. Goldenstein, and R. K. Hanson, "Compact optical probe for flame temperature and carbon dioxide using interband cascade laser absorption near 4.2μm," Combust. Flame **178**, 158–167 (2017).
37. P. Nau, P. Kutne, G. Eckel, W. Meier, C. Hotz, and S. Fleck, "Infrared absorption spectrometer for the determination of temperature and species profiles in an entrained flow gasifier," Appl. Opt. **56**, 2982–2990 (2017).
38. L. H. Ma, L. Y. Lau, and W. Ren, "Non-uniform temperature and species concentration measurements in a laminar flame using multi-band infrared absorption spectroscopy," Appl. Phys. B **123**, 83 (2017).
39. C. Wei, D. I. Pineda, L. Paxton, F. N. Egolfopoulos, and R. M. Spearrin, "Mid-infrared laser absorption tomography for quantitative 2d thermochemistry measurements in premixed jet flames," Appl. Phys. B **124**, 123 (2018).
40. C. Wei, D. I. Pineda, C. S. Goldenstein, and R. M. Spearrin, "Tomographic laser absorption imaging of combustion species and temperature in the mid-wave infrared," Opt. Express **26**, 20944–20951 (2018).
41. R. Villarreal and P. L. Varghese, "Frequency-resolved absorption tomography with tunable diode lasers," Appl. Opt. **44**, 6786–6795 (2005).
42. X. Liu, G. Zhang, Y. Huang, Y. Wang, and F. Qi, "Two-dimensional temperature and carbon dioxide concentration profiles in atmospheric laminar diffusion flames measured by mid-infrared direct absorption spectroscopy at 4.2 μm," Appl. Phys. B **124**, 61 (2018).

Optics EXPRESS

43. H. Li, X. Zhou, J. B. Jeffries, and R. K. Hanson, "Sensing and Control of Combustion Instabilities in Swirl-Stabilized Combustors Using Diode-Laser Absorption," AIAA J. **45**, 390–398 (2007).
44. P. E. Best, P. L. Chien, R. M. Carangelo, P. R. Solomon, M. Danchak, and I. Ilovici, "Tomographic reconstruction of FT-IR emission and transmission spectra in a sooting laminar diffusion flame: Species concentrations and temperatures," Combust. Flame **85**, 309–318 (1991).
45. D. R. Snelling, K. A. Thomson, G. J. Smallwood, and O. L. Gülder, "Two-dimensional imaging of soot volume fraction in laminar diffusion flames," Appl. Opt. **38**, 2478–2485 (1999).
46. C. J. Dasch, "One-dimensional tomography: a comparison of Abel, onion-peeling, and filtered backprojection methods," Appl. Opt. **31**, 1146 (1992).
47. K. J. Daun, K. A. Thomson, F. Liu, and G. J. Smallwood, "Deconvolution of axisymmetric flame properties using Tikhonov regularization," Appl. Opt. **45**, 4638–4646 (2006).
48. S. Johnson, "Faddeeva W function implementation," .
49. H. Wang, C. Law, and T. Lieuwen, "Linear response of stretch-affected premixed flames to flow oscillations," Combust. Flame **156**, 889–895 (2009).
50. P. Preetham, S. K. Thumuluru, T. Lieuwen, and H. Santosh, "Linear Response of Laminar Premixed Flames to Flow Oscillations: Unsteady Stretch Effects," J. Propuls. Power **26**, 524–532 (2010).